Chapter 5

Self-Supported De-Alloyed Nickel based Amorphous Steel Ribbons for Enhanced Electro-catalysis

5.1. Introduction

A scalable synthesis of nanoporous $(Ni_{87}Fe_4Cr_9)_{78}Si_8B_{14}$ amorphous ribbon with active α-$Ni(OH)_2$ phase for efficient oxygen evolution (OER) and methanol oxidation reaction (MOR) is reported in this chapter. Surface de-alloying in 0.5 M HNO_3 for 60 minutes generates a dense, ~2 µm-thick (NiCr) oxy/hydroxide network with a nanoporous structure. The resulting electrocatalyst exhibits an over-potential of 290 mV at 10 mA cm^{-2}, a Tafel slope of 53 mV dec^{-1}, and ECSA of 132 cm^2 in 1 M KOH. For MOR in 1 M KOH + 1 M MeOH, the treated catalyst demonstrates a low onset potential of 1.35 V vs. RHE at 10 mA cm^{-2}, with a Tafel slope of 52 mV dec^{-1} and double-layer capacitance of 66 µF. This study presents a reproducible strategy for designing high-performance electrocatalysts for OER and MOR applications.

5.2. Results and Discussion

Figure 5.1a compares the XRD patterns of melt-spun NiFeCrSiB amorphous ribbons (R0), characterized by a broad hump, and surface de-alloyed ribbon (R60), which exhibit multiple diffraction peaks in the 2θ range of 10–40° in addition to the amorphous hump. The distinct peaks correspond to the (003), (006), and (101) planes of α-$Ni(OH)_2$ (JCPDS: 38-0715), indicating the formation of an electrocatalyst on the ribbon surface during the de-alloying process. SEM micrographs of the R60 reveal a dense, interconnected network

of granular $Ni(OH)_2$ electrocatalyst with an average particle size of ~2.2 µm (**Figure 5.1b-d**). The inter-connected architecture creates dense network of nano-porous region (30-200 nm) and surface roughness desirable for electro catalysts.

Elemental mapping of the $Ni(OH)_2$ granules on the ribbon surface shows clear elemental redistribution between the bare ribbon and the hydroxide-rich regions (**Figure 5.1e**). Notably, the electrocatalyst region exhibits partial Ni depletion, Cr and O enrichment, and a complete absence of Fe, suggesting the presence of Cr in the $Ni(OH)_2$ region. As-cast ribbons (20×10 mm^2) were chemically de-alloyed in 0.5 M HNO_3 for 0 to 120 min to optimize electrocatalytic performance.

Figure 5.2a shows the XPS surface survey spectra, confirming the presence of Ni, Cr, Fe, and O in both R0 (as-cast) and R60 (surface-treated) samples. In R0, the Ni 2p3/2 peak at 852.9 eV indicates elemental Ni with minimal oxidation, suggesting limited electrocatalytic activity due to the absence of Ni-O species. In contrast, R60 exhibits a Ni 2p3/2 peak shift at 855.9 eV, indicating oxidation to $Ni(OH)_2$, as confirmed by deconvolution (**Figure 5.2b**).

The O 1s spectra of R0 shows a single peak at 531.5 eV, corresponding to adsorbed oxygen, with no significant oxygenated species. Whereas, R60 displays deconvoluted O 1s peaks at 531.5 eV (adsorbed oxygen) and 532 eV ($Ni(OH)_2$), confirming the formation of active oxygenated Ni species (**Figure 5.2c**). Cr 2p spectra reveal partial oxidation of Cr (0) to Cr (III) in R0 and in R60 (**Figure 5.2d**).

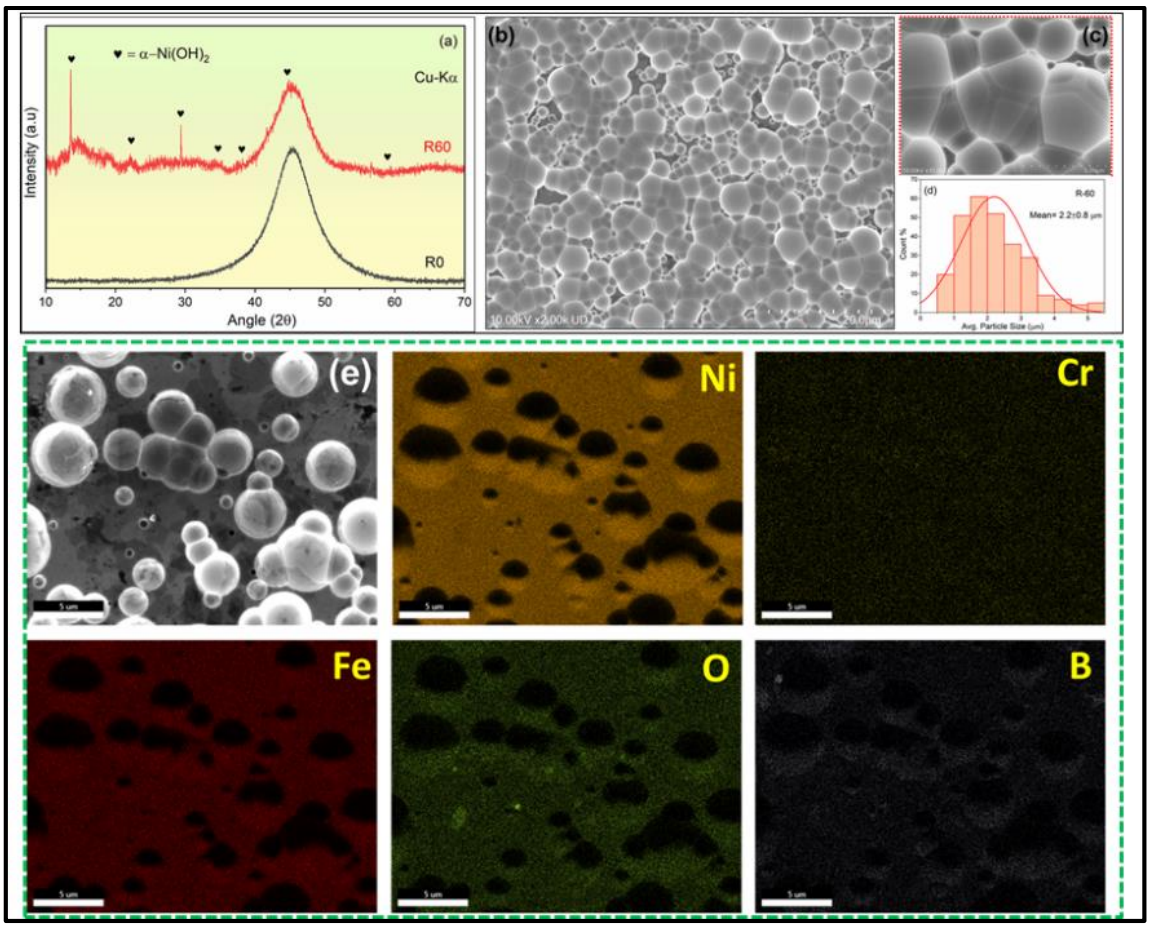

Figure 5.1- (a) XRD patterns, (b,c) SEM micrographs, (d) particle size distribution, and (e) elemental mapping of $Ni(OH)_2$ electrocatalysts formed on the R60 ribbon surface.

Fe 2p spectra show no significant changes between R0 and R60, suggesting Fe remains unaffected by the surface treatment. These findings show surface de-alloying in R60 induces significant Ni and Cr oxidation, forming active oxygenated species that enhance electrocatalytic performance, while Fe remains unchanged.

5.3. OER and MOR performance

As-spun and de-alloyed ribbon catalysts were systematically examined for OER in 1 M KOH. Cyclic voltammetry (CV) and linear sweep voltammetry (LSV) plots shown in **Figure 5.3a-b** compares the performance of R0 and optimized R60 ribbon.

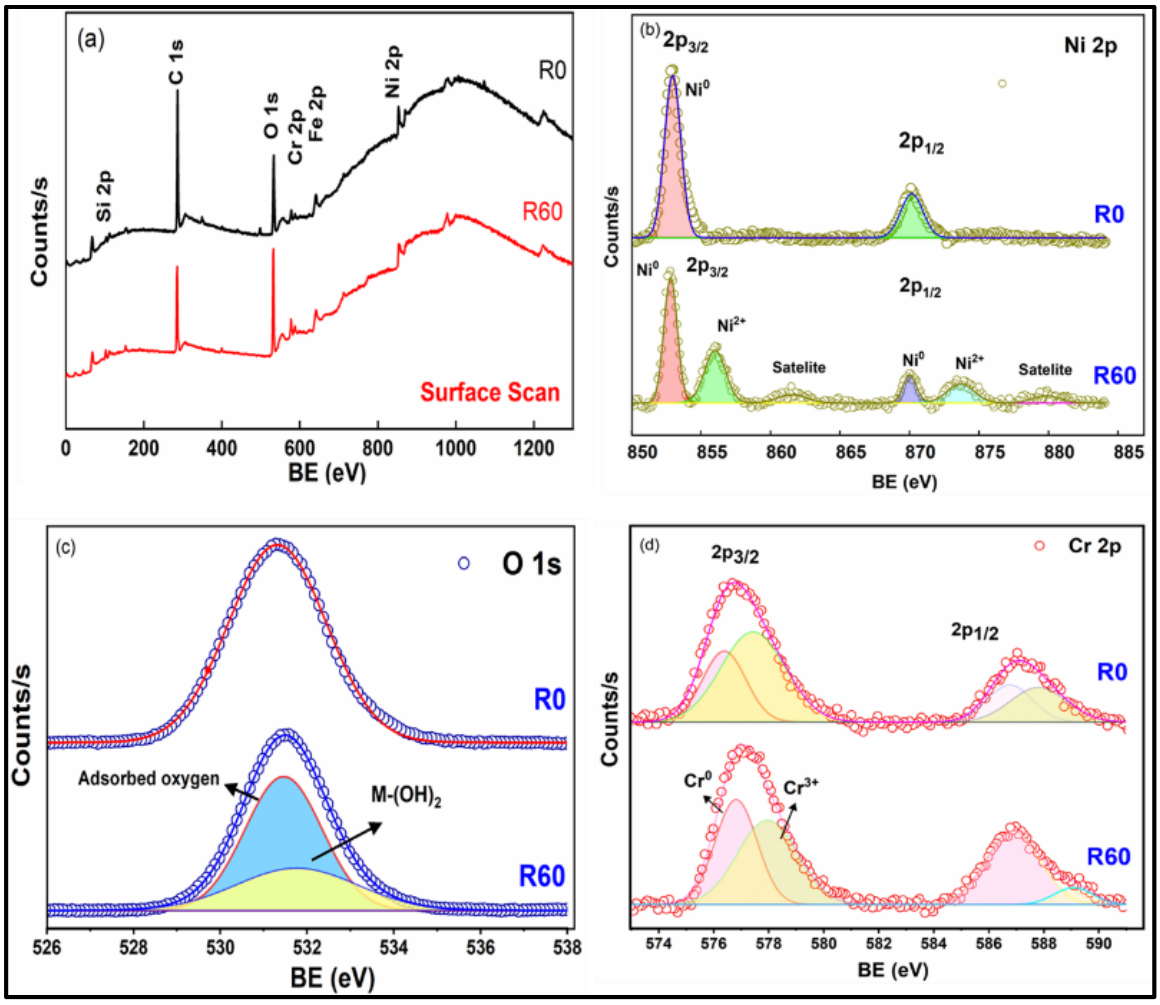

Figure 5.2- XPS spectra comprising (a) Surface scan and core level spectra of (b) Ni 2p, (c) O 1s, and (d) Cr 2p of as-cast (R0) and de-alloyed (R60) ribbon.

The R60 exhibits superior performance, achieving an over-potential of 290 mV at 10 mA cm^{-2}, compared to R0 (356 mV at 10 mA cm^{-2}). The markedly lower Tafel slope of 53 mV dec^{-1} (R60) compared to 84 mV dec^{-1} in R0, evidences accelerated OER kinetics (**Figure 5.3c**). These findings indicate lower activation energy and enhanced reaction kinetics for R60, likely due to the formation of optimally sized Ni-hydroxide species during surface de-alloying.

Nyquist plots (**Figure 5.3d**), fitted with an equivalent circuit model, revealed a charge transfer resistance (R_{ct}) of 1.65 Ω (R60), significantly lower than 5.4 Ω (R0), confirming an improved charge transfer mechanism. In addition, Figure 5.7 highlights the higher double layer capacitance (C_{dl}) for R60 (5.3 mF) compared to R0 (0.07 mF) and an excellent long-term stability, highlighting the enhanced OER performance.

For MOR, evaluated in 1M KOH + 1M MeOH vs. Hg/HgO, R60 exhibits an onset potential of 1.35 V vs. RHE (vs. 1.42 V for R0) and achieved 10 mA cm^{-2} at 1.38 V vs. RHE, compared to 1.52 V for R0, indicating earlier methanol oxidation onset (**Figure 5.4a-b**). The Tafel slope for R60 exhibits 52 mV dec^{-1}, markedly lower than R0 (**Figure 5.4c**), suggesting faster reaction kinetics of MOR. EIS plot denotes the charge transfer resistance (R_{ct}) of R60 (0.44 Ω), much lower than R0 (3.2 Ω), reflecting faster charge transfer kinetics, surpassing its OER performance (**Figure 5.4d).** In continuation, Figure in 5.8 shows the higher C_{dl} for R60 (66µF) than R0 (21µF) confirming its superior MOR performance and stability.

Overall, surface de-alloyed R60 shows enhanced electrocatalytic efficiency and kinetics for both OER and MOR compared to R0 and similar kinds of reported electrocatalysts (**Table 5.1**). The combination of long-term stability, mechanical adhesion, corrosion resistance, and flexibility makes them attractive compared to other binder-free electrocatalysts [114].

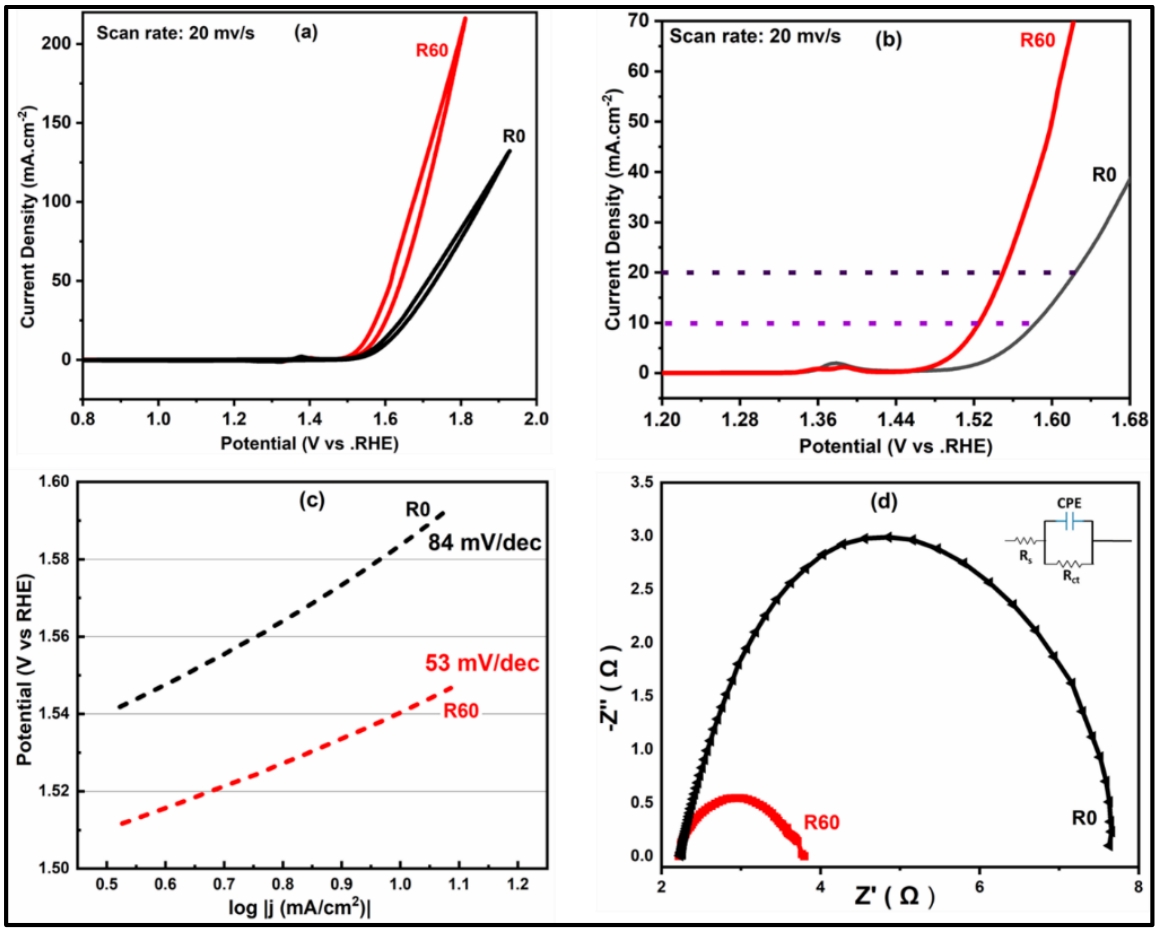

Figure 5.3- Electrochemical characterization of R0 and R60 in 1 M KOH (a) CV (b) Linear polarization (c) Tafel plot and (d) Nyquist plot.

The nitric acid de-alloying process in the present study induces dense Ni-hydroxide formation along with nanoscale surface porosity and roughness, effectively nanostructuring the catalyst surface. This is evidenced by the increased ECSA for OER (132 cm^2 for R60 vs. 1.8 cm^2 for R0). Moreover, the Cr enrichment in the hydroxide region indirectly influences the preferential formation and enhanced catalytic activity of $Ni(OH)_2$[115]. Interestingly, a change in surface treatment of the same alloy ribbon from cathodic corrosion to acid de-alloying, results in the formation of a coarser particle

morphology that ranges from nano to micron-scale [116]. This shift not only alters the particle structure but also facilitates a preferential substitution of iron (Fe) for chromium (Cr) in $Ni(OH)_2$, significantly influencing the electrocatalytic performance [117]. Chemically de-alloying in 0.5 M HNO_3 for 0–120 min to optimize electrocatalytic performance is shown in **Figure 5.5**. Additional EDS area spectrum results were shown in supplementary data **Figure 5.6.** In addition, **Figure 5.7** shows the double layer capacitance (C_{dl}) values for R60 (5.3 mF) and R0 (0.07 mF) along with long-term stability. **Figure 5.8** shows the C_{dl} for R60 (66µF) higher than R0 (21µF) confirming the MOR performance towards DMFC application along with stability.

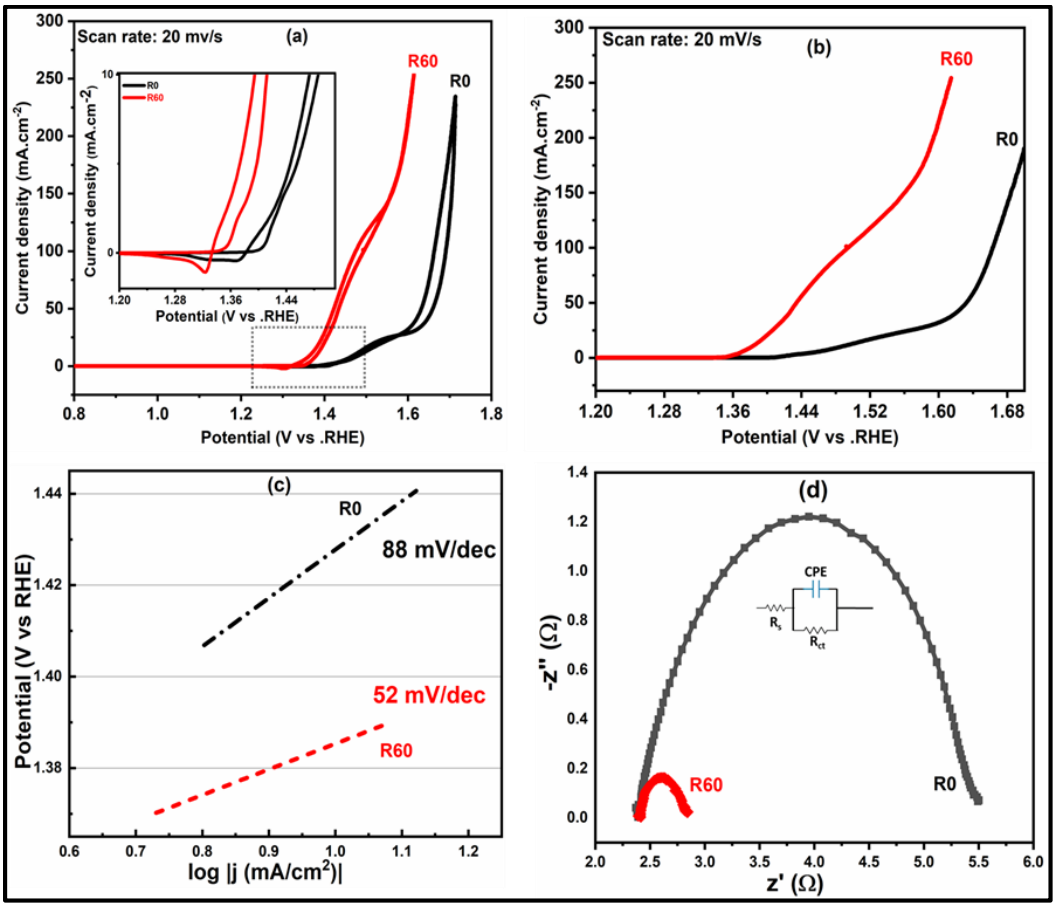

Figure 5.4- Electrochemical characterization of R0 and R60 in 1 M KOH + 1 M MeOH (a) CV (b) Linear polarization (c) Tafel plot and (d) Nyquist plot.

5.4. Summary

Our findings highlight the scalable synthesis strategy for self-supported electrocatalysts through the surface de-alloying of amorphous alloy ribbon. The dense network of hydroxide with nano-porous architecture leads to superior OER and MOR performance. The de-alloyed electrocatalyst showed higher ECSA and lower R_{ct} suggesting enrichment of active sites and improved charge transfer kinetics resulting from redistribution of electrons. The present work reports a holistic design for developing noble-metal-free, self-supported and binder-free electro catalysts for cost-effective and scalable energy solutions.

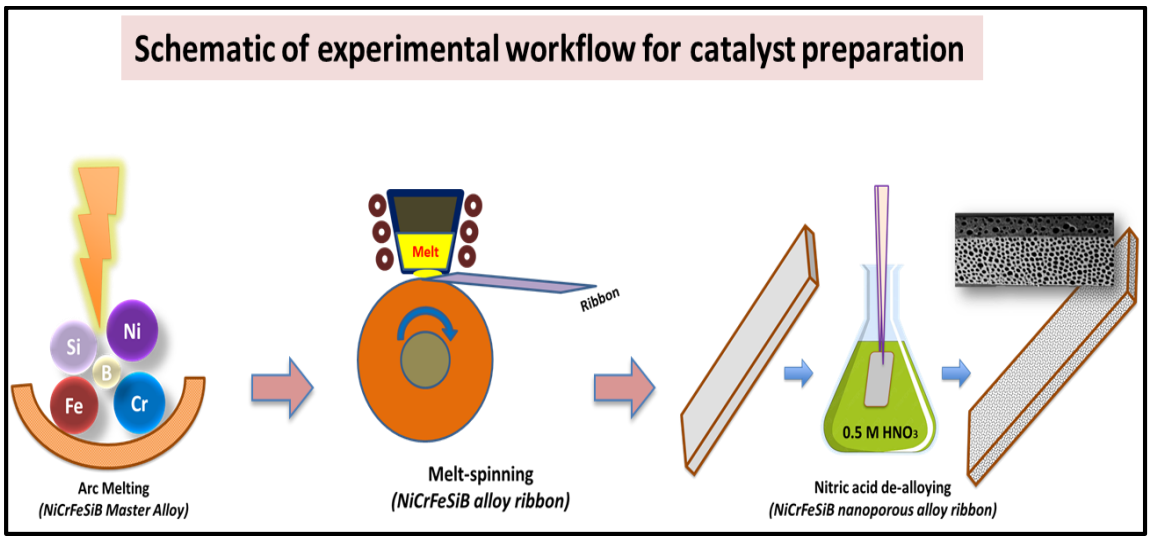

Figure 5.5- Schematic of experimental workflow for the preparation of nano-porous, self-standing Ni-based catalyst.

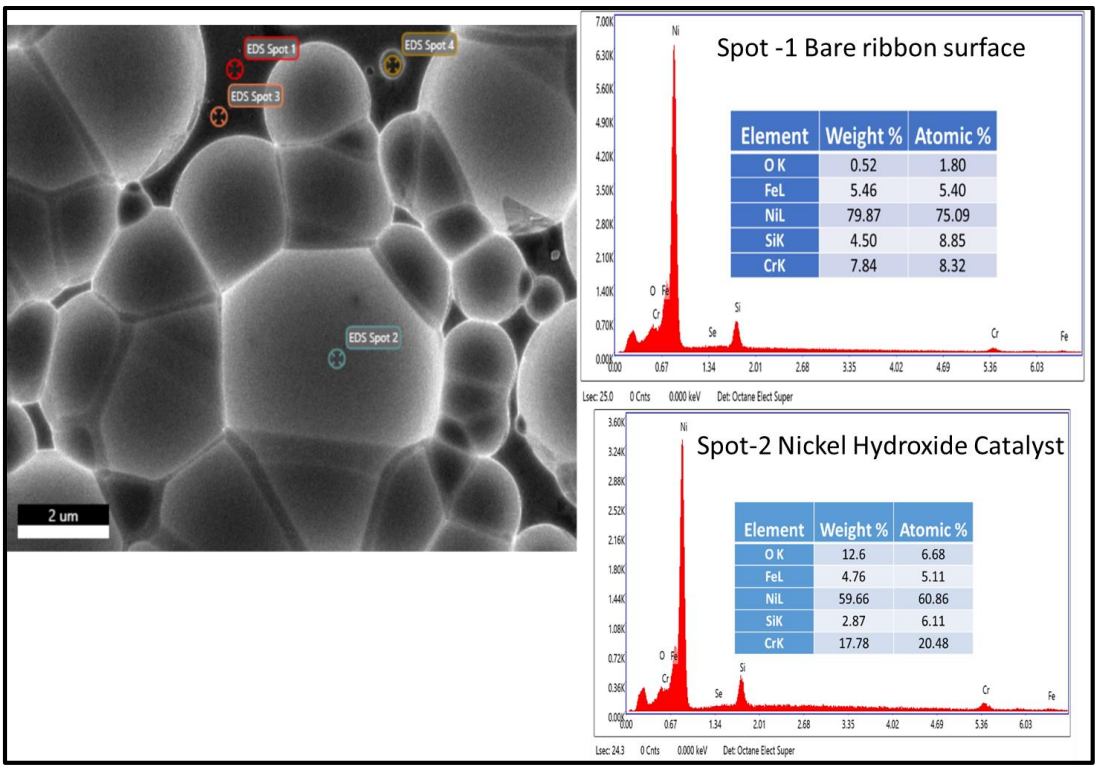

Figure 5.6- SEM EDS spectra on bare(R0) and catalyst (R60) surface depicting elemental re-distribution, mainly enrichment of O and Cr and dilution of Ni after de-alloying process.

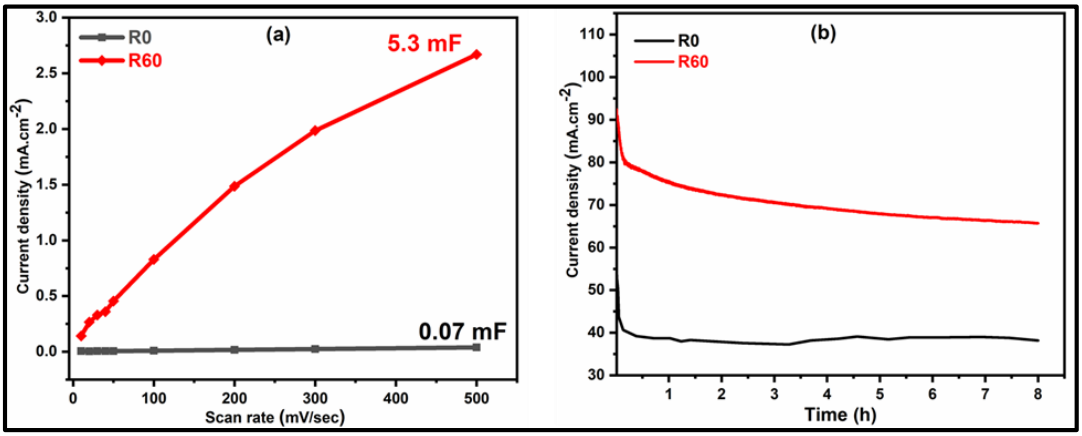

Figure 5.7- Electrochemical characterization plots of as-cast (R0) and de-alloyed (R60) in 1 M KOH (a) Double layer capacitance and (b) Chronoamperometry at 1.62 V (Vs. RHE).

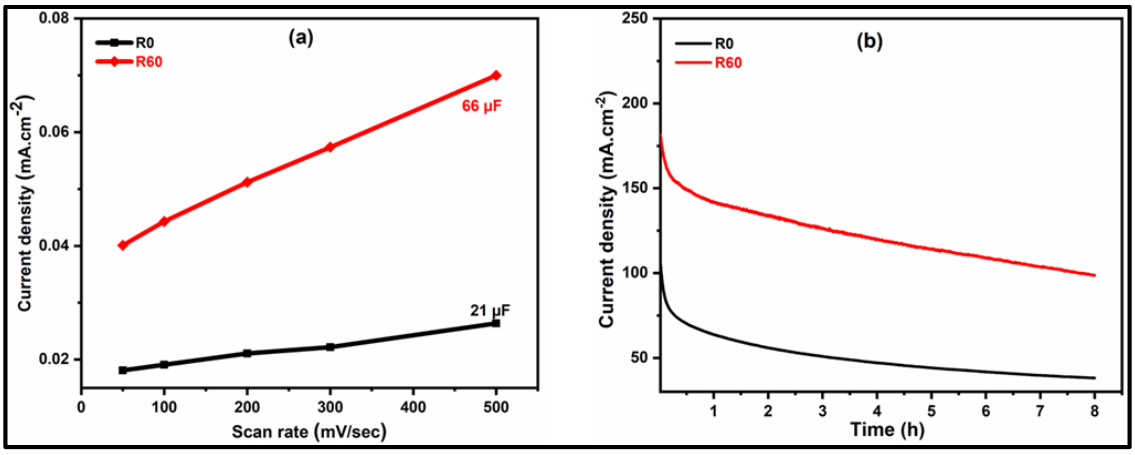

Figure 5.8- Electrochemical characterization plots of as-cast (R0) and de-alloyed (R60) in 1 M KOH + 1 M MeOH (a) Double layer capacitance and (b) Chronoamperometry at 1.5 V (Vs. RHE).

Table 5.1- OER studies comparison with counterpart reported transition metal-based Electro-catalysts in KOH. Over-potential values reported at current density of 10 mA cm^{-2} for comparison.

Catalyst	**Phase**	**η (mV)**	**Tafel slope (mV/dec)**	**Electrolyte**	**References**
$(Ni_{87}Fe_4Cr_9)_{78}Si_8B_{14}$ – R60	**Amo**	**290**	**53**	**1 M KOH**	**This work**
np-$Fe_{40}Ni_{37}Nb_3P_{13}C_7$	Amo	276	35.9	1 M KOH	[68]
FeCoCrNi	Cryst.	300	51.4	1 M KOH	[110]
NiPdP	Cryst.	340	46	1 M KOH	[111]
FeCoNiB	Amo	274	38	1 M KOH	[112]
NiFeB	Amo	319	56	1 M KOH	[113]
$Ni_{50}Fe_{25}B_{15}Si_7P_3$	Amo	306	45.1	1 M KOH	[61]
$Fe_{25}Co_{25}Ni_{25}Mo_9P_8B_8$	Amo	281	36.44	1 M KOH	[63]
$Ni_{50}Fe_{25}B_{15}Si_7P_3$	Amo	269	40.5	1 M KOH	[61]
np-NiFeMoP	Amo	197	41.2	1 M KOH	[62]
$Fe_{78}Si_9B_{13}$	Amo	356	45	1 M KOH	[65]
np- $(Ni_{87}Fe_4Cr_9)_{78}Si_8B_{14}$	Amo	295	51	1 M KOH	[116]
Amo= Amorphous ; Cryst. = crystalline ; np = nano-porous					